Earth, Planets and Space

FULL PAPER Open Access

Surface deformation of Asama volcano, Japan, detected by time series InSAR combining persistent and distributed scatterers, 2014–2018

Xiaowen Wang[1,2*], Yosuke Aoki[1] and Jie Chen[3]

Abstract

Asama volcano is one of the most active volcanoes in Japan. Spatially dense surface deformation at Asama volcano has rarely been documented because of its high topography and snow cover around the summit. This study presents the first interferometric synthetic aperture radar (InSAR) observation of ground deformation at Asama volcano with 120 Sentinel-1 SAR images from both ascending and descending tracks and 20 descending ALOS-2 images acquired between 2014 and 2018. We exploited both persistent and distributed scatterers to overcome decorrelation of SAR signals and applied a three-dimensional unwrapping method to retrieve the displacement time series efficiently. Our observations reveal an asymmetric deformation around the volcano with two main deformation regions on the northeast and southeast flanks, respectively. The northeast flank (NEF) exhibits line-of-sight (LOS) extensions in all the three SAR datasets with maximum velocities of − 14, − 10, and − 12 mm/year for the descending ALOS-2, ascending, and descending Sentinel-1 measurements, respectively. The southeast flank (SEF) shows LOS extensions in the ascending observations and LOS shortening in the descending observations with velocities between − 12 and 9 mm/year. Decomposition of the LOS displacements reveals nearly pure subsidence at the NEF, while the SEF exhibits a substantial eastward component as well as subsidence. Comparisons of the vertical subsidence at two continuous GNSS stations near the summit crater with our InSAR observations indicate small discrepancies smaller than 4 mm/year. We interpreted that the subsidence at the NEF of Asama is primarily due to the hydrothermal activity, while the deformation at SEF is plausibly due to flank instability. We highlight that efforts should be taken to monitor the slope instability at Asama volcano in the future.

Keywords: Asama volcano, InSAR, Volcano deformation, Persistent scatterers, Distributed scatterers, Slope instability

Introduction

Asama volcano is an andesitic composite volcano and one of the most active volcanoes in Japan. Asama volcano has been active for about 100,000 years and repeatedly erupted every several years in history (Aoki et al. 2013). The recent eruptions at Asama volcano were in 2004, 2008, 2009, 2015, and 2019. An eruption at Asama volcano has the potential of posing volcanic hazards to the Tokyo metropolitan area, which is about 160 km southeast of the volcano with a population of more than 20 million. For instance, the 2004 eruption in Asama volcano produced large ash clouds and led to ashfall in the Tokyo metropolitan area (Tsunematsu et al. 2008). For this reason, monitoring the activity of Asama volcano is essential for mitigating volcanic hazards during future large eruptions.

Geodetic measurements of surface deformation at active volcanoes can provide important clues for assessing volcanic activity (Pinel et al. 2014). Leveling surveys were repeated 22 times at and around Asama volcano between 1902 and 2005 (Murase et al. 2007). Continuous global navigation satellite system (GNSS) observations at Asama volcano have also been implemented since the mid-1990s (Takeo et al. 2006; Aoki et al. 2013). These geodetic measurements have revealed that the deformation pattern of Mt Asama is temporally variable. Leveling

*Correspondence: insarwxw@gmail.com
[1] Earthquake Research Institute, The University of Tokyo, Tokyo, Japan
Full list of author information is available at the end of the article

benchmarks at the eastern flank of the volcano have shown minor subsidence between 1935 and 1939 and apparent uplift during 1939 and 1950, while the leveling surveys at the southeastern flank exhibited significant uplift between 1902 and 1952 and moderate subsidence between 1952 and 2004 (Murase et al. 2007). Murase et al. (2007) described these vertical displacements as due to the deflation and inflation of two pressure sources beneath Mt Asama. Temporal variations in baseline length between continuous GNSS stations around Asama volcano have also exhibited frequent alternation between contraction and expansion (Aoki et al. 2013). Contraction of the GNSS baseline has been observed preceding both the 2004 and 2009 eruptions and been interpreted as degassing from previously intruded magma (Kazahaya et al. 2015).

Although conventional geodetic measurements from leveling and GNSS have provided crucial insights into the deformation pattern and magmatic activity of Asama volcano, a detailed characterization of surface deformation at the volcano is still lacking. One important reason is that the GNSS stations are sparsely distributed around the volcano with only two continuous GNSS sites around the summit (KAHG and KAWG in Fig. 1). While interferometric synthetic aperture radar (InSAR) has proven to be a useful tool for mapping ground deformation with high spatial resolution and precision (Hooper et al. 2012; Pinel et al. 2014), InSAR has rarely been applied to Asama volcano. Decorrelation of InSAR due to several factors such as the steep topography, dense vegetation, and snow cover around the summit have limited the application of InSAR to monitor deformation at Asama volcano (Pinel et al. 2014; Remy et al. 2015).

Considerable efforts have been made to overcome phase decorrelation of InSAR and increase measurement points by exploiting a subset of pixels with stable phase such as persistent scatterer (PS) or distributed scatterer (DS) from repeated SAR images (Crosetto et al. 2016). A classical method that exploits both PS and DS from SAR images is Stanford Method for Persistent Scatterers (StaMPS) method developed by Hooper et al. (2004). This method assumes that ground deformation is spatially correlated and implements spatial filtering with a boxcar window to distinguish stochastic noise phase from other phase components. However, such spatial filtering may bias interferometric phase because the scattering patterns of neighboring pixels may be heterogeneous (Parizzi and Brcic 2011; Jiang et al. 2015). The advantage of StaMPS is that it does not rely on any strong a priori assumptions of the temporal evolution of deformation by implementing a three-dimensional (3D) unwrapping method, facilitating the efficient detection of non-linear surface motion over time. As an alternative

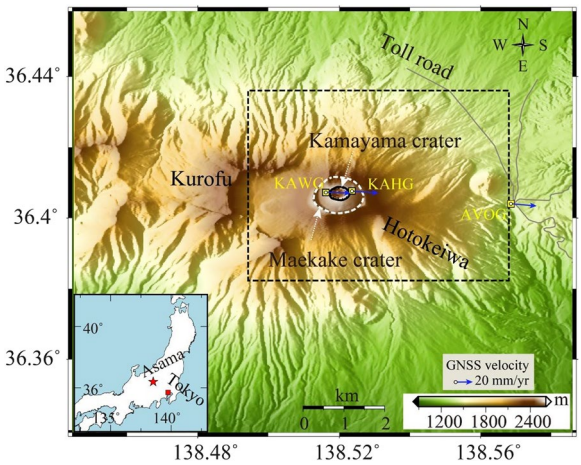

Fig. 1 The topography map of Asama volcano with an insert showing the locations of Mt. Asama and Tokyo. The white dashed line and black solid line on the summit indicate the Maekake and the Kamayama craters, respectively. Two old volcanoes, Kurofu and Hotokeiwa, lay to the west and on the southeast flank of Maekake volcano, respectively. The yellow squares indicate the location of the three GNSS stations, whereas the station AVOG is located at the eastern base of the volcano and the other two stations (KAWG and KAHG) are located on the edges of the summit Kamayama crater. The blue vectors indicate the horizontal displacement velocities of GNSS stations. The dashed black box indicates the region where our InSAR analysis focused on, namely, the geographical extents of Figs. 2, 5, 6, and 7

way to increase measurement points, Ferretti et al. (2011) proposed a method called SqueeSAR™, in which a triangulation algorithm is implemented to "optimize" interferometric phase using all possible interferograms. While SqueeSAR™ can increase measurement points remarkably, the phase triangulation procedure is time consuming, because $(N(N-1))/2$ interferograms are required from N SAR images.

In this study, we attempted to characterize the modern surface deformation of Asama volcano with repeated Sentinel-1 and ALOS-2 SAR images acquired between 2014 and 2018. Considering the severe decorrelation of SAR signals at the volcano, we developed a new InSAR processing procedure by taking advantage of the preexisting methods StaMPS and SqueeSAR™. First, we selected PS and DS following a method similar to Ferretti et al. (2001, 2011), with some modifications for a more robust selection of PS and DS. We then retrieved the displacement time series by applying the 3D unwrapping method on the selected pixels within the framework of StaMPS (Hooper et al. 2004, 2008). The proposed method takes advantage of SqueeSAR™ for increasing measurement points and StaMPS for obtaining ground deformation products more efficiently. We also investigated possible mechanisms to account for the observed deformation

with independent geological data and other geophysical observations around the volcano.

Geological background

Asama volcano is a complex volcano consisting of Kurofu, Hotokeiwa, and Maekake volcanoes from west to east (Fig. 1). Kurofu volcano, the oldest edifice, collapsed eastward and formed the horseshoe-shaped caldera approximately 24,000 years ago (Aramaki 1963). After the activity of Kurofu Volcano ceased, the eruption center shifted to the east, and the Hotokeiwa volcano formed around 17,000–11,000 years ago (Aramaki 1963). The most recent volcanism was at the Maekake volcano, on which the Kamayama crater remains active at present. The latest major eruptions with Volcanic Explosivity Index (VEI; Newhall and Self 1982) of 4–5 took place in 1108, 1128, and 1783 AD (Aramaki 1963). The eruptions have become less explosive during the last few decades with several moderate-sized eruptions of VEIs 2 in 1982, 1983 and 2004. More recently, minor eruptions with VEIs of 1 took place in 2008, 2009, and 2015.

The highest point of Asama Volcano is the summit of the Kamayama crater (Fig. 1) at about 2560 m above sea level. The Kamayama crater has a diameter of about 500 m in the east–west direction and 440 m in the north–south direction (Fig. 1). The topography of Asama volcano is steep with an elevation difference of 1150 m between the summit and a GNSS site AVOG at the volcanic base ~ 4 km to the east of the summit. The slope angles of the volcano mainly range between 20° and 50°, and the western flank is steeper than the eastern flank (Aoki et al. 2013).

Geological mapping shows that Asama volcano is mainly covered by six types of pyroclastic flow that were emplaced during past eruptions (Fig. 2a). By a chronological sequence, the geological deposits are the KCN formed during the activity of Kurofu volcano, the HLF formed during the activity of Hotokeiwa volcano, the BIG formed during the 1108 explosive eruption, and the ACN, ALF, and AIG erupted during the 1783 eruption. The lava flows of the 1783 eruption cover the summit area and most of the north and east flanks (Hayakawa 2006).

SAR data

We collected a total of 140 SAR images comprising 120 C-band Sentinel-1 images and 20 L-band ALOS-2 images to detect the surface deformation at Asama volcano between 2014 and 2018. The Sentinel-1 images are acquired from two paths: 58 images from the descending path and 62 images from the ascending path. The ALOS-2 images are acquired from the descending path 19. The Sentinel-1 SAR satellites have a temporal sampling interval of 12 or 24 days, while the ALOS-2 images are uneven sampled with adjacent intervals from 14 to 224 days. The short sampling rate of Sentinel-1 SAR images has a potential of maintaining SAR coherence even if the wavelength of radar wave is short (~ 5.5 cm). The ALOS-2 SAR images with a longer wavelength (~ 24 cm) are less affected by temporal decorrelation of the SAR signal. Table 1 lists the detailed information of the SAR data. The acquisition dates of the SAR images are listed in Additional file 1: Tables S1–S3.

Dense vegetation covers Asama volcano. Figure 2b shows the Normalized Difference Vegetation Index (NDVI) (Rouse et al. 1974) calculated from the cloud-free

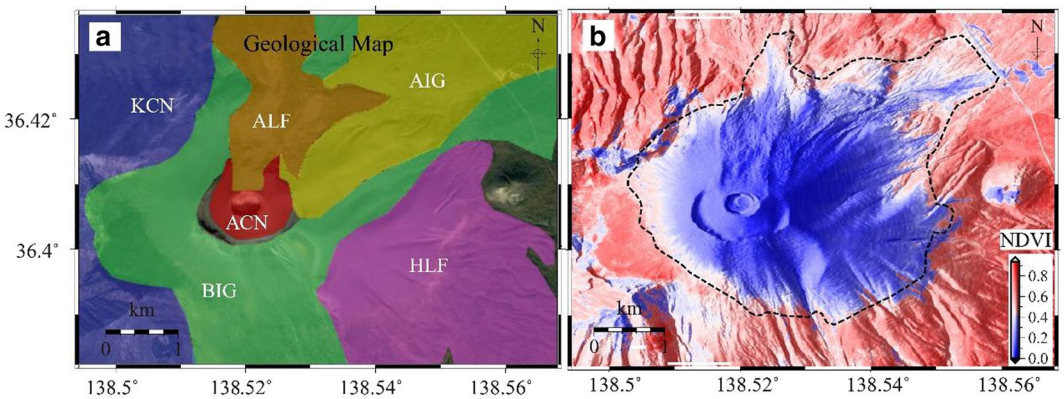

Fig. 2 The geological map (**a**) and the Normalized Difference Vegetation Index (NDVI) map (**b**) around Asama volcano. The annotations in (**a**) indicate different types of geological deposits, namely, *KCN* Kurofu cone formed about 24,000 years ago, *HLF* Lava of Hotokeiwa cone formed about 11,000 years ago, *BIG* Oiwake ignimbrite formed during the 1108 explosive eruption, *ACN* Kamayama scoria cone, *ALF* Oni Oshidashi lava flow, *AIG* Agatsuma ignimbrite. All the ACN, ALF, and AIG were formed during the 1783 eruption. The blue and red color in **b** indicate the increase in Vegetation Coverage Index

Table 1 SAR data used in this study

Satellite	Time span	Path number	No. of images	Off-nadir angle (°)	Azimuth angle (°)	Resolution (Rg × Azi m)	No. of interferogram
ALOS-2	20141028–20180814	19	20	36.2	− 169.7 (descending)	1.4 × 2.1	75
Sentinel-1A	20150411–20180302	119	58	33.8	− 166.8 (descending)	2.3 × 14.0	220
Sentinel-1B	20150430–20180303	39	62	33.8	− 10.5 (ascending)	2.3 × 14.0	187

Sentinel-2 image acquired on 21 May 2017. Previous studies have shown that the densities of PS and DS are highly correlated with the NDVI value (Cigna et al. 2014). Given this insight, our study mainly focuses on this region of NDVI lower than 0.4 around the summit as circled by the dashed line in Fig. 2b because the dense vegetation beyond the region prevents us from obtaining reliable measurements due to the loss of coherence of SAR images. Additional file 1: Figure S1 shows an example of coherence from two Sentinel-1 images acquired in the summer of 2017, which demonstrates significant coherence loss outside the circled region. Although the coherence of ALOS-2 data is generally better than the Sentinel-1 data, the ALOS-2 data have a poor temporal resolution, which may degrade the quality of deformation estimate over highly vegetated regions. Therefore, we focus on the region where both the C-band Sentinel-1 and ALOS-2 data can reliably obtain surface deformation, forming a cross-validation between the two SAR sensors.

SAR data processing

The basic idea of multi-temporal InSAR analysis is to select a subset of pixels (PS or DS) based on certain statistics such as their amplitude or phase over multiple SAR images, and then estimate the mean velocities and the evolution of displacement on these selected pixels (Osmanoğlu et al. 2016). Figure 3 shows the procedure of multi-temporal InSAR analysis by jointly analyzing PS and DS as we propose in this study. Main steps of the proposed method include the generation of interferograms, selection of the PS and DS, three-dimensional phase unwrapping, and the calculation of the mean velocity and displacement time series. We will present these main steps in detail in this section.

Generation of SAR interferograms

We generated SAR interferograms with small temporal and perpendicular baselines. This reduced the number of interferograms and the processing time compared with SqueeSAR™ (Ferretti et al. 2011) that makes full use of all the possible interferograms. All the SAR pairs from ALOS-2 images have perpendicular baselines smaller than 400 m, and only those with temporal separation less than 400 days are selected to generate interferograms. For each path of the Sentinel-1 data, we selected two groups of interferograms: one group includes pairs with the maximum temporal separation of 60 days and perpendicular baseline of 200 m; the other group includes pairs with the maximum temporal separation of 400 days and maximum perpendicular baseline of 100 m. We adopted such selection criteria for Sentinel-1, because Asama volcano is covered with snow most of the time in winter, leading to significant temporal decorrelation for some winter interferograms. We added inter-annual summer interferograms

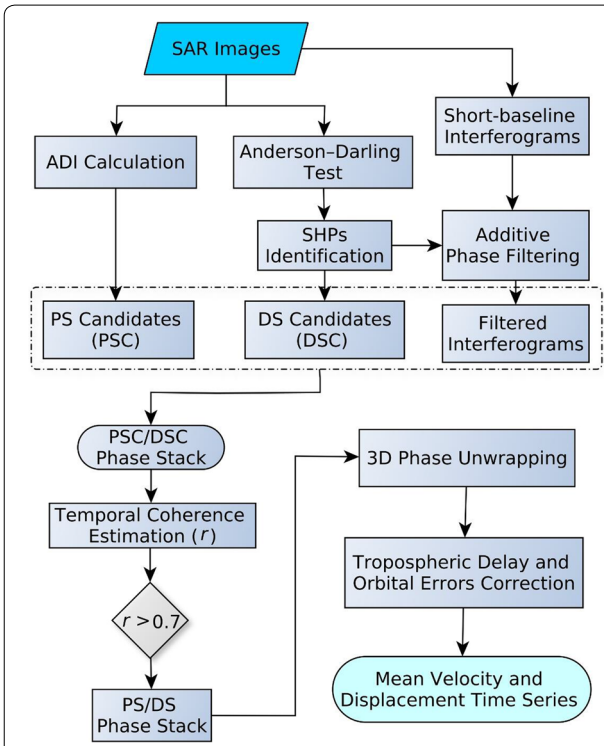

Fig. 3 Flowchart of the SAR data processing in this study. Note the acronyms with *ADI* Amplitude Dispersion Index, *SHP* statistically homogeneous pixels, *PS* persistent scatterers, *DS* distributed scatterers, *3D* three-dimensional

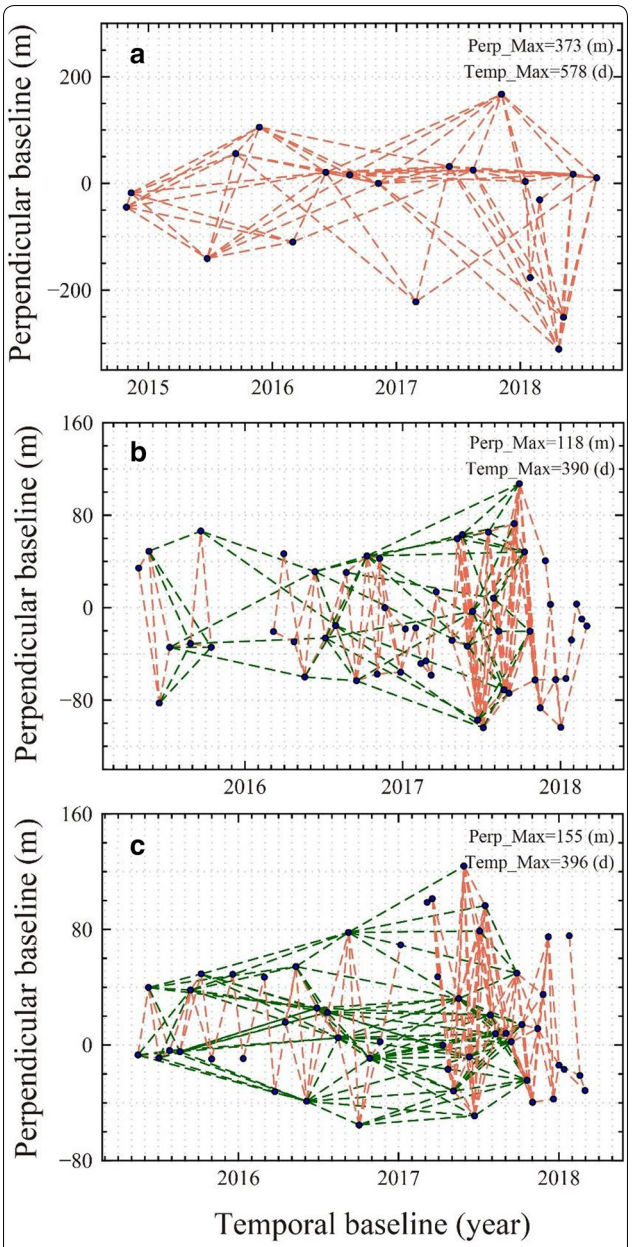

Fig. 4 Temporal and perpendicular baselines for the **a** ALOS-2, **b** ascending Sentinel-1, and **c** descending Sentinel-1 image pairs. The blue circles represent individual SAR acquisitions, and the lines connecting them represent the pairs from which small baseline interferograms are formed. The red lines in (**b**) and (**c**) indicate pairs with temporal separation less than 60 days and the green lines indicate those less than 400 days

for the Sentinel-1 data to avoid unconnected SAR images. Figure 4a–c show the networks for the ALOS-2 and ascending and descending Sentinel-1 images, respectively.

We used the GAMMA software to generate interferograms (Wegmüller and Werner 1997). A digital elevation model (DEM) with a 10-m resolution provided by Geospatial Information Authority of Japan was employed to correct for topographic phase.

PS and DS selection

Identifying PS and DS candidates

The first step of PS/DS selection is to determine PS candidates (PSC) or DS candidates (DSC) according to the statistical patterns of amplitudes of a set of SAR images. We selected PSC based on the amplitude dispersion index (ADI, D_A) defined as (Ferretti et al. 2001):

$$D_A = \frac{\sigma_A}{\mu_A} \tag{1}$$

where μ_A and σ_A are the mean and standard deviation of series of amplitude values, respectively. Pixels with ADI smaller than 0.4 are considered as PSC (Hooper et al. 2004).

The selection of DSC starts from the determination of statistically homogeneous pixels (SHPs), whose amplitudes share similar statistical characteristics over time (Ferretti et al. 2011). For an arbitrary pixel, goodness-of-fit testing is usually employed to determine its surrounding SHPs within a specific window (Jiang et al. 2015; Parizzi and Brcic 2011). Several testing methods such as the Kolmogorov–Smirnov test (Stephens, 1970), Anderson–Darling test (Papoulis 1965), and the generalized likelihood ratio test (Pettitt 1976) have been proposed in recent years. Here we adopt the Anderson–Darling test to select SHPs because it has proven to be more robust than the other methods given a large stack of SAR images (Parizzi and Brcic 2011). The Anderson–Darling two-sample test is a nonparametric test with the test statistic A^2 defined as (Parizzi and Brcic 2011):

$$A^2 = \frac{M}{2} \sum_{x \in \{x_{p,i}, x_{q,i}\}} \frac{\left(\hat{F}_p(x) - \hat{F}_q(x)\right)^2}{\hat{F}_{pq}(x)\left(1 - \hat{F}_{pq}(x)\right)} \tag{2}$$

where $x_{p,i}$ and $x_{q,i}$ are the amplitude time series of two pixels p and q, $i = 1, 2, ..M$, and M is the number of SAR images, $\hat{F}_p(x)$ and $\hat{F}_q(x)$ are empirical cumulative distribution functions of amplitudes for the pixels p and q, $\hat{F}_{pq}(x)$ is empirical distribution function of the pooled distribution $\{x_{p,i}, x_{q,i}\}$. The two pixels p and q are considered homogenous if the calculated A^2 for them is less than a threshold value. After the identification of SHPs, we estimated the adaptive coherence for each pixel based on its surrounding SHPs within a square window of 7 pixels. The pixels with mean coherence larger than 0.2

are then considered as PSC. Additional file 1: Figure S2 shows the number of SHPs for each pixel from three SAR datasets.

We also implemented adaptive multi-looking in each interferogram to enhance the signal-to-noise ratio of the interferometric phase. The idea of adaptive multi-looking is to average a given pixel only with neighboring SHPs instead of a rectangular averaging (Jiang et al. 2015). Considering that the summit crater of Asama volcano has a diameter of only a few hundred meters, we employed a small window size (3×3) when implementing the adaptive multi-looking. Compared with the phase triangulation method adopted in SqueeSAR™ (Ferretti et al. 2011), which also aims at improving phase quality, adaptive multi-looking is more efficient without the requirement of using all possible interferograms. Taking the pair 20150123–2012021 from ascending Sentinel-1 (path 39) data as an example, Fig. 5a, b shows the initial interferometric phase and that after adaptive multi-looking, indicating a significant improvement of the phase quality.

Selection of PS and DS

With the identified PSC and DSC, we selected pixels with a stable phase over time as PS and DS. A good indicator of phase stability (Tizzani et al. 2007) is the temporal coherence of each PSC and DSC as estimated as follows.

Assuming that M interferograms were generated following the criteria described in "Generation of SAR interferograms" section and unwrapped independently using the 3D unwrapping method (Hooper et al. 2004), for a given pixel with coordinates (x, r), the unwrapped phase of the *kth* interferogram computed from the SAR acquisitions at times T_B and T_A can be expressed as:

$$\begin{aligned}\delta\phi_k(x,r) &= \phi(t_B,x,r) - \phi(t_A,x,r) \\ &= \frac{4\pi}{\lambda}[d(t_B,x,r) - d(t_A,x,r)] + \Delta\phi_k^{\text{topo}}(x,r) \\ &+ \Delta\phi_k^{\text{orb}}(x,r) + \Delta\phi_k^{\text{noise}}(x,r)\end{aligned} \tag{3}$$

where $k = 1, 2, \ldots M$, λ is the SAR wavelength, $\phi(t_B,x,r)$ and $\phi(t_A,x,r)$ represent phase at the two acquisitions, $d(t_B,x,r)$ and $d(t_A,x,r)$ are the cumulative LOS displacements at t_B and t_A with respect to the first acquisition time of SAR images. $\Delta\phi_k^{\text{topo}}(x,r)$ and $\Delta\phi_k^{orb}(x,r)$ are phase errors due to uncertainties in DEM and SAR orbital parameters, respectively, in which the former can be modeled as $\frac{4\pi}{\lambda}\frac{B_{\perp_k}\Delta h(x,r)}{R\cdot\sin(\theta)}$ and the latter can be estimated and removed with a second-order polynomial fitting. $B_{\perp_k}$, R, Δh, and θ represent the perpendicular baseline, slant range, DEM uncertainty, and SAR off-nadir angle, respectively.

We solved Eq. (3) with singular value decomposition by setting the cumulative displacements and DEM error as unknown parameters. Then, we re-constructed the interferometric phase ($\delta\tilde{\phi}_k$) which only consists of deformation, topographic error, and orbital error. The difference between the initial and re-constructed phase represents the noise level of SAR phase history, from which we can

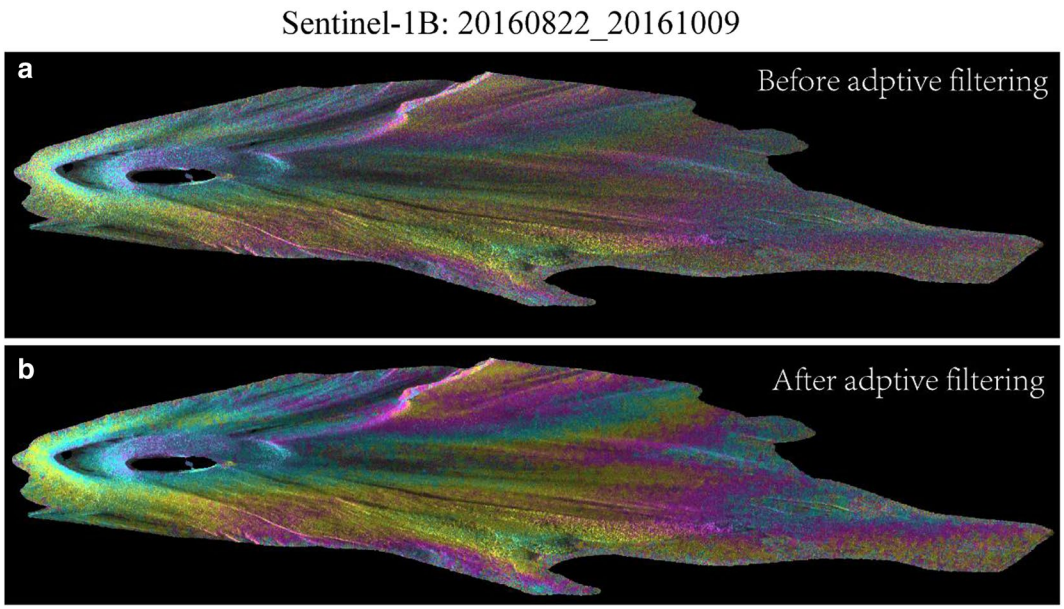

Fig. 5 The Sentinel-1B interferogram 20160822–20161009 before (**a**) and after (**b**) adaptive multi-looking based on the statistically homogeneous pixels (SHPs). Note the images are in radar coordinates

calculate the temporal coherence (r_t) for each PSC and DSC:

$$r_t = \frac{\left|\sum_{k=1}^{M} \exp\left[j\left(\delta\emptyset_k - \delta\tilde{\phi}_k\right)\right]\right|}{M} \quad (4)$$

Both the $\delta\emptyset_k$ and $\delta\tilde{\phi}_k$ need to be wrapped phase to calculate r_t which ranges between 0 and 1 (Tizzani et al. 2007). We selected the PSC and DSC with temporal coherence higher than 0.7 as PS and DS for further time series analysis.

Retrieving mean deformation rates and displacement time series

Once the selection of PS and DS is completed, we can obtain a phase stack on the selected pixels. We then imported the phase stack into the StaMPS software for further InSAR time series analysis, followed by steps of 3D phase unwrapping, correction for phase errors including orbital and topographic errors and tropospheric delay, estimation of mean deformation velocity, and displacement time series retrieving (Hooper 2008).

As a remark, we used the Toolbox for Reducing Atmospheric InSAR Noise (TRAIN) provided by Bekaert et al. (2015) to correct for tropospheric phase delay. We tested three independent correction methods within TRAIN to determine which method provides the best performance of tropospheric phase correction. They are, namely, (1) the linear phase-elevation fitting method (Zebker et al. 1994; Beauducel et al. 2000), (2) the predictive tropospheric estimates from ERA-Interim (ERA-I) atmospheric reanalysis data (Dee et al. 2011), and (3) the GACOS phase delay products from the operational high-resolution European Centre for Medium Range Weather Forecasts data (Yu et al. 2018). Previous studies have shown that none of these methods have been entirely successful in correcting for tropospheric errors in SAR interferograms, and the performance of each method highly depends on the local topo-climate conditions (Pinel et al. 2011; Kinoshita et al. 2012; Remy et al. 2015).

Results

Comparison of atmospheric corrections

Figure 6a shows the mean LOS velocities from the ascending Sentinel-1 images (path 39) without

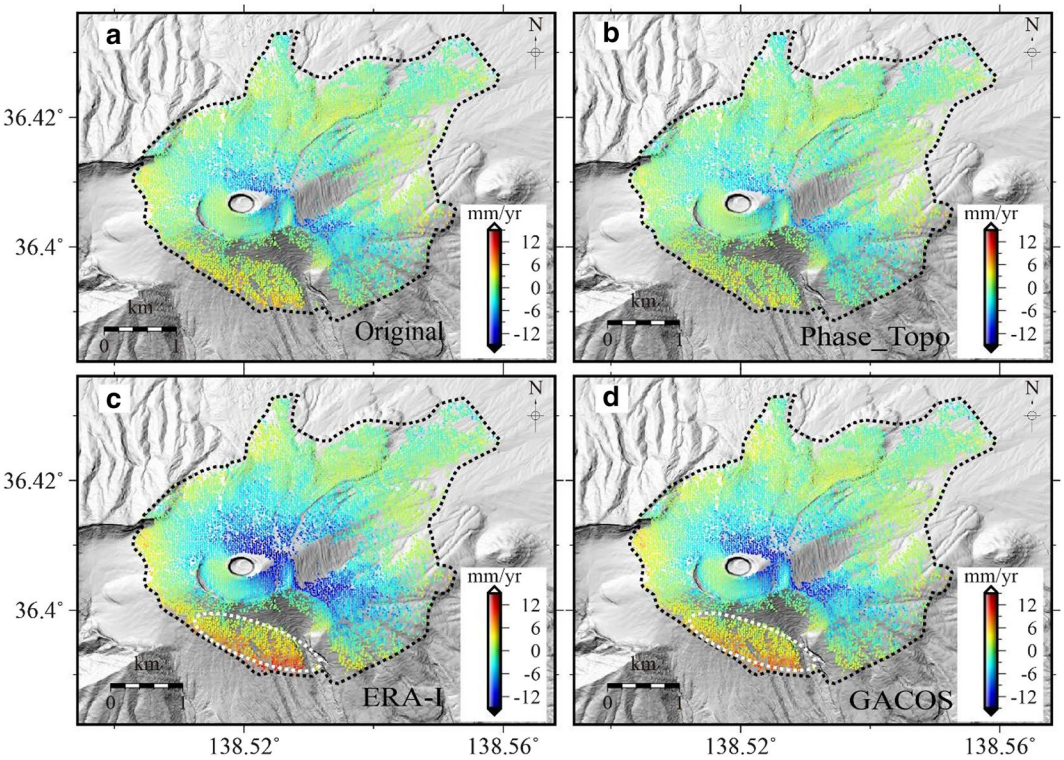

Fig. 6 Comparisons of mean velocities from ascending Sentinel-1 (path 39) before and after the tropospheric delay correction. **a** Mean LOS velocities without correction; **b**, **c** mean velocities corrected for tropospheric delay by **b** the elevation-phase linear fitting method, **c** the ERA-I weather model, and **d** the GACOS weather model. The white dashed polygons in **c** and **d** indicate the regions showing significant LOS shortening after the correction

corrections, while Fig. 6b–d are those after the correction for the tropospheric delay with the three correction methods as described in "Retrieving mean deformation rates and displacement time series" section. Slight differences exist between the mean velocities with the three different correction methods. The deformation field after corrections with weather models shares similar deformation patterns with broad LOS shortening around the volcanic base and evident LOS extension near the summit. Especially, an area showing anomalous range shortening appears on the southwest flank of the volcano more clearly after the corrections with weather models (see white polygons in Fig. 6c, d). However, the different deformation patterns between the volcanic base and summit are inconsistent with the GPS observations (see "Validation of the InSAR measurements" section).

We calculated the correlation coefficient between the interferometric phase and elevation to evaluate the performance of the corrections. The correlation coefficient between the elevation and the phase before corrections is 0.19, while those after the tropospheric correction by phase-elevation fitting, ERA-I, and GACOS are 0.14, 0.34, and 0.28, respectively. The linear fitting gives the smallest correlation coefficient between phase and elevation, while, unexpectedly, the weather model data does not reduce the correlation coefficient. The relatively large correlation coefficients from weather model data are probably because there is significant difference in spatial resolution between the SAR images and weather models, which are 75 km and 14 km for ERA-I and GACOS, respectively. Additionally, the acquisition time of a given SAR image relative to the time period of the weather model would also impact the quality of the correction (Murray et al. 2019), particularly over a high mountain area like Mt Asama with highly variable tropospheric conditions. Although the linear fitting may also remove the elevation-correlated displacements, this would not significantly affect the interpretation of deformation at Mt Asama because the correlation coefficient between the elevation and the uncorrected phase is smaller than 0.2. Therefore, we employed the phase-elevation linear fitting method to correct for the tropospheric phase delay to generate the deformation field.

Deformation field

With the SAR processing procedure presented in "SAR data processing" section, we successfully detected ground deformation at Asama volcano with high spatial resolution. The number of PS detected from the ALOS-2, ascending Sentinel-1, and descending Sentinel-1 images are 2112, 697, and 531, respectively, while the number of DS from the three datasets are 16942, 12455, and 12358, respectively. Both the numbers of PS and DS identified from ALOS-2 images are higher than those from Sentinel-1 because of the higher coherence with ALOS-2 images. We identified much more DS than PS, indicating that the measurement points were remarkably improved by the inclusion of DS. As an example, Additional file 1: Figure S3 shows the distributions of PS and DS from the ascending Sentinel-1 images (path 39). Although only hundreds of PS were identified from the ascending Sentinel-1, we included the PS in the further analysis because the PS are mainly located near the summit where the coherence loss is significant.

Figure 7a shows the topography with a resolution of 10 m used in this study, in which the black dotted line indicates the extent of our measurement points. Figure 7b–d show the mean LOS velocities from the ALOS-2, ascending Sentinel-1, and descending Sentinel-1 images, respectively. Additional file 1: Figure S4 shows the standard deviations of the LOS velocities estimated by the percentile bootstrapping method in StaMPS (Efron and Tibshirani 1986; Shamshiri et al. 2018). The reference point (white circle in Fig. 7a) was selected on the road at the eastern flank of the volcano, where the deformation there was assumed to be stable over the observation period. The standard deviations of the LOS velocities at the reference point from the three SAR datasets are all smaller than 3 mm/year.

The blue and red color in Fig. 7b–d represent the LOS extension and shortening, respectively. All the LOS measurements from the three datasets exhibit asymmetric patterns with deformation predominantly at the eastern flank of the volcano. Deformation at Asama volcano can be roughly divided into two sections: the northeast flank (NEF) and the southeast flank (SEF) with areas of approximately 3.68 km^2 and 2.14 km^2, respectively (Fig. 7b–d). The NEF exhibits LOS extension from all the three datasets with the maximum LOS extension rates from the ALOS-2, ascending Sentinel-1, and descending Sentinel-1 images -14, -12, and -10 mm/year, respectively. The displaced region at SEF forms a fan shape with apparent LOS shortening and extension from descending and ascending paths, respectively. The maximum mean velocities at SEF from the three datasets range between -12 and 9 mm/year.

Figure 8 shows LOS velocities along the P_1P_1' and P_2P_2' rectangular profiles with a width of 60 m (Fig. 7a) encompassing the NEF and SEF, respectively. The topography along the two profiles is also shown in Fig. 8 (right axis) by gray lines. The displacements along P_1P_1' shows that areas close to the summit show relatively larger LOS extension rates with negligible velocities at about 1.2 km from the summit and further. The displacements along P_2P_2' exhibit a more scattered pattern than those along P_1P_1' with maximum velocities at the central part

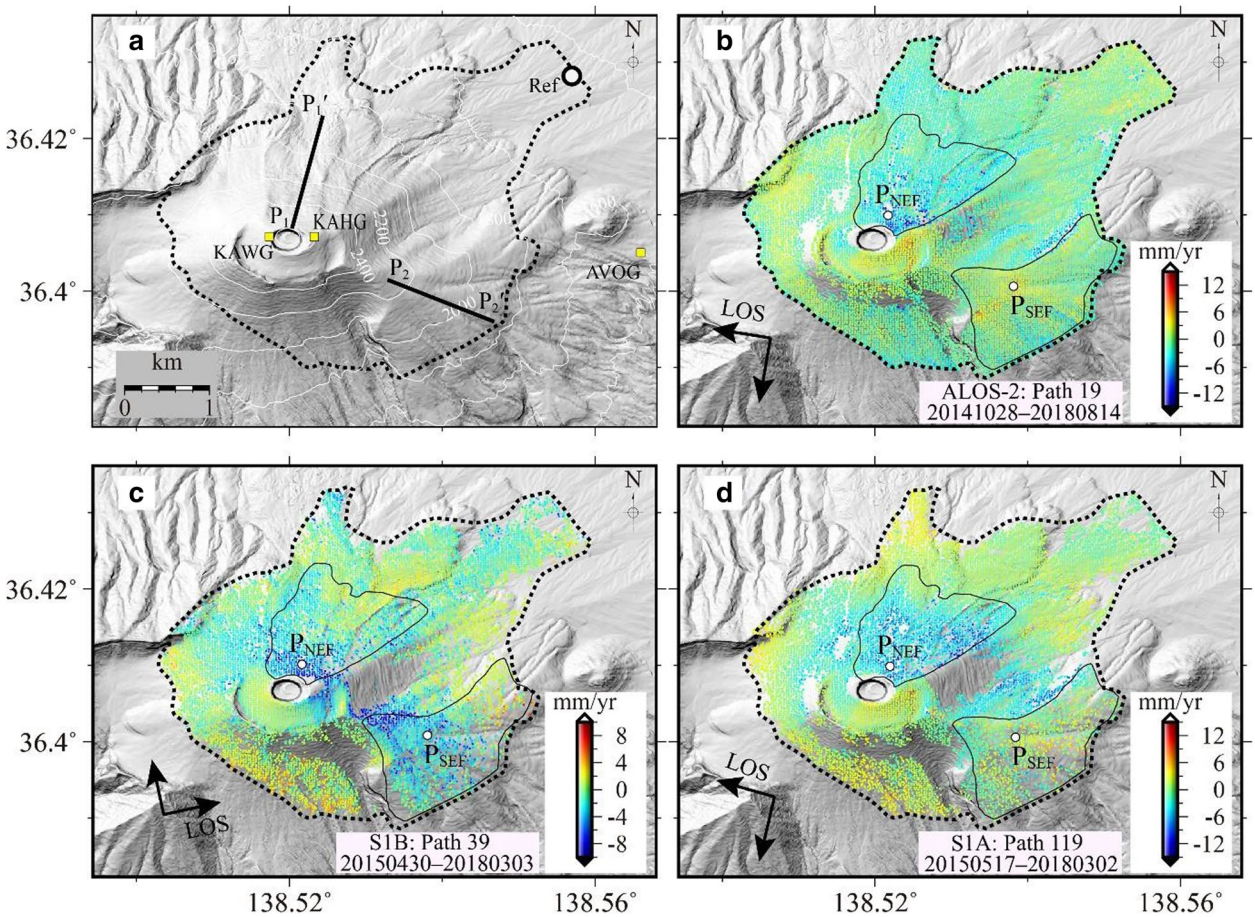

Fig. 7 **a** Topography around Asama volcano. Two solid lines indicate profiles whose LOS displacements are shown in Fig. 8. The mean LOS velocities from the **b** ALOS-2, **c** ascending Sentinel-1, and **d** descending Sentinel-1 images. Two deformation regions at the northeast and southeast of the volcano are circled by solid black lines in **b**–**d**. P_{NEF} and P_{SEF} are the two points selected for plotting the displacement time series in Fig. 9. Black dotted lines in all panels indicate the area with NDVI value smaller than 0.4 as shown in Fig. 2b. The time span in each sub-figure indicates the observation period

of the slope. The deformation rate along P_2P_2' from the ascending path (path 39) is much higher than that from the descending paths, implying significant east–west movement.

Figure 9 shows the temporal evolution of LOS displacements at P_{NEF} and P_{SEF}, the locations of which are denoted in Fig. 7b–d. All the time series exhibit approximately linear trend over the entire period, implying that the mechanisms controlling the deformation do not change over the observation period. We did not detect significant deformation anomaly associated with a VEI 1 eruption in June 2015, suggesting that the mass transfer during this episode was limited.

We also calculated the quasi-vertical and quasi-east–west velocities by decomposing the LOS velocities from the three SAR datasets (Additional file 1: Fig. S5). The north–south component is ignored due to its insensitivity to LOS measurements by InSAR (e.g., Wright et al. 2004). Statistics of the quasi-vertical and east–west velocities show that 65% of the points within NEF show subsidence, while 59% of the points within SEF show a sliding deformation pattern. Table 2 shows the decomposed velocities at the selected points P_{NEF} and P_{SEF}. Uncertainties of the estimates were calculated by the law of error propagation (Cecchi 1991). The time series at P_{NEF} exhibit apparent subsidence of about -6.0 ± 0.2 mm/year with a minor east–west component. The time series at P_{SEF} exhibit the eastward velocity of 6.7 ± 0.08 mm/year and minor subsidence of -2.1 ± 0.05 mm/year. We thus suggest that the deformation at the NEF is dominated by subsidence, while the deformation at SEF is presumably in the slope direction. A possible mechanism to explain the observed deformation at NEF and SEF will be discussed in "Possible mechanism for the observed deformation" section.

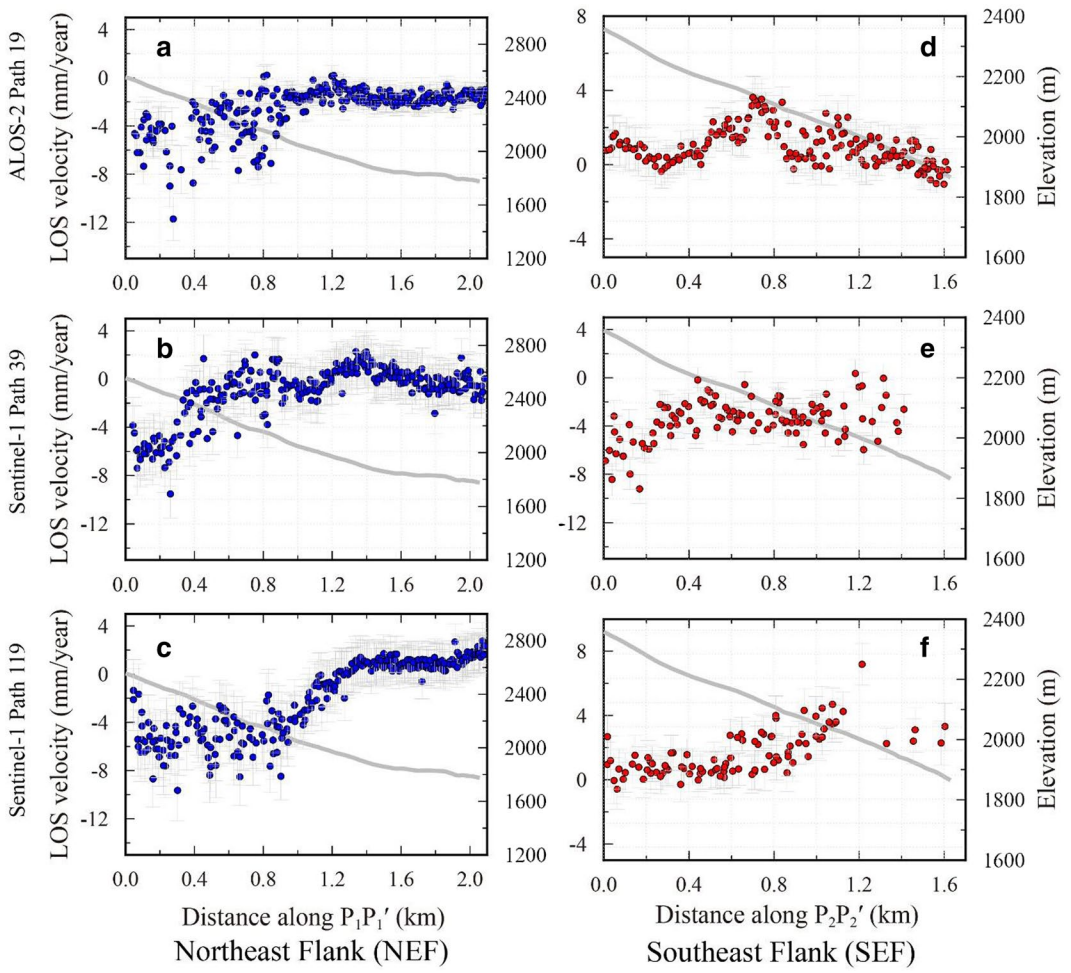

Fig. 8 LOS velocities along the two profiles P_1P_1' and P_2P_2' (Fig. 7a) that encompass NEF and SEF, respectively. LOS velocities along P_1P_1' from the **a** ALOS-2, **b** ascending Sentinel-1, and **c** descending Sentinel-1 images. **d**–**f** Similar to **a**–**c** but for the profile P_2P_2'. Note the positive velocity represents LOS shortening, and the negative velocity represents LOS extension. Error bars represent the estimated uncertainties (Additional file 1: Fig. S4) for deformation velocities

Discussion

Validation of the InSAR measurements

Quantifying the errors of InSAR measurements is difficult, primarily because the tropospheric and ionospheric phase delays cannot be completely circumvented (e.g., Remy et al. 2015). In this study, we used linear regression to reduce the tropospheric delay correlated with topography, which may also partially remove the topography dependent deformation (Zebker et al. 1994; Beauducel et al. 2000). The displacement time series at points P_{NEF} and P_{SEF} from some SAR images (e.g., Fig. 9b, d, e) slightly exhibit a seasonal fluctuation, probably due to unmodelled seasonal tropospheric delays.

We validated our InSAR observations with GNSS measurements from three continuous GNSS stations (KAWG, KAHG, and AVOG in Fig. 1). Additional file 1: Figure S6 shows the displacement time series in east–west, north–south, and vertical directions at these three GNSS sites. The displacements at KAHG and AVOG cover the whole period of our InSAR observation, while the records at KAWG are unavailable after January 2017 due to a power outage. To compare the GNSS measurements with our InSAR observations, we calculated the vertical velocities of KAHG and KAWG (Fig. 10) between October 2014 and March 2018 relative to AVOG. We did not include the horizontal displacements of the GNSS stations for comparison, because the relative horizontal displacements between KAHA/KAWG and AVOG are much smaller than vertical displacements (see Fig. 1). The mean vertical velocities at KAHG and KAWG are −5.6 and −1.1 mm/year (Fig. 10), respectively, which are comparable with our InSAR observations with a maximum difference of 3.2 mm/year (Table 2). The GNSS measurements

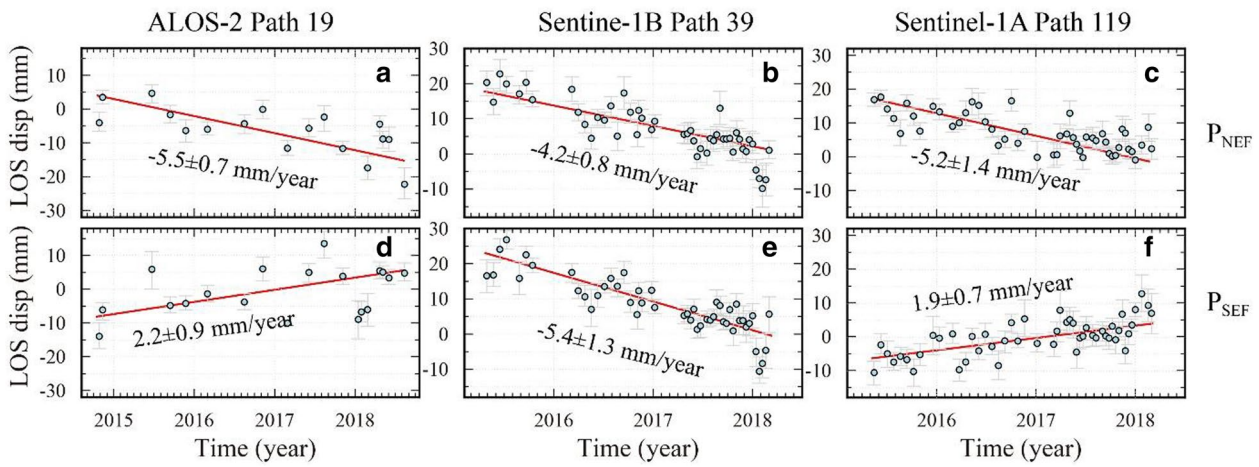

Fig. 9 Time series of LOS changes at the two selected points P_{NEF} and P_{SEF} (Fig. 7). **a–c** Time series at P_{NEF} from the ALOS-2, ascending Sentinel-1, and descending Sentinel-1 images. **d–f** Similar to **a–c** but for the point P_{SEF}. Error bars are standard deviations estimated over the points located within a window with size of 3 × 3 pixels

Table 2 Velocities in the LOS, east–west, and vertical components at four representative points

Points	ALOS-2 (path 19)	Sentinel-1B (path 39)	Sentinel-1A (path 119)	East–west	Vertical
P_{NEF}	−5.5±0.7	−4.2±0.8	−5.2±1.4	−0.8±0.3	−6.0±0.2
P_{SEF}	2.2±0.9	−5.4±1.3	1.9±0.7	6.7±0.08	−2.1±0.05
KAHG	−7.1±1.3	−8.5±2.9	−4.9±2.0	2.1±2.4	−8.8±1.6
KAWG	−1.2±0.7	1.6±1.2	0.8±0.5	−1.7±2.0	0.9±1.3

P_{NEF} and P_{SEF} are located at the center of NEF and SEF (Fig. 7a), respectively; KAHG and KAWG are GNSS stations located at the edge of the Kamayama summit crater (Fig. 1). All the values are in mm/year

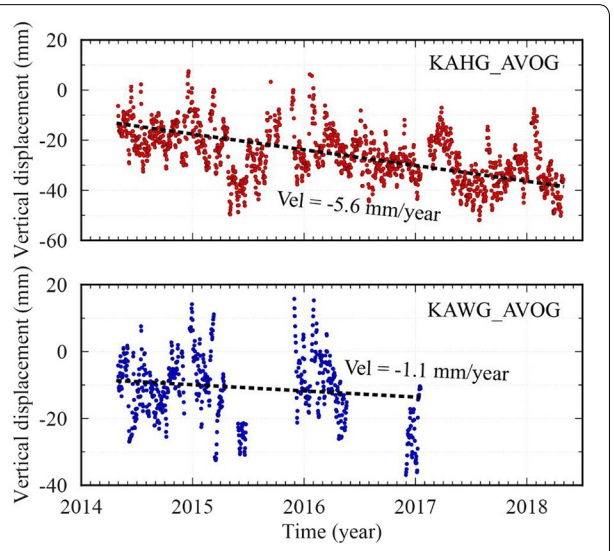

Fig. 10 Vertical displacement time series at two GNSS stations KAHG and KAWG with respect to the station AVOG between October 2014 and March 2018. The vertical displacement rate at each station is also annotated

also confirm that the deformation mainly took place on the eastern flank of the volcano. We then projected the 3D displacements from KAHG at the east side of the volcano into the radar LOS direction to compare with InSAR measurements. The comparisons (Fig. 11) indicate that the displacement time series from both ascending Sentinel-1 (path 39) and descending ALOS-2 (path 19) are consistent with the GNSS measurements.

Comparison with historical deformation records at Asama volcano

Compared with the historical deformation patterns recorded at Asama volcano, our InSAR observations do not reveal an apparent transition between inflation and deflation. The temporal evolution of displacements from InSAR exhibits a linear trend at both the NEF and SEF of the volcano ("Deformation field" section). One possible reason for the constant temporal patterns in the observed deformation could be the dominance of shallow mechanisms (e.g., thermal contraction, flank instability) rather than deeper magma pressurization/

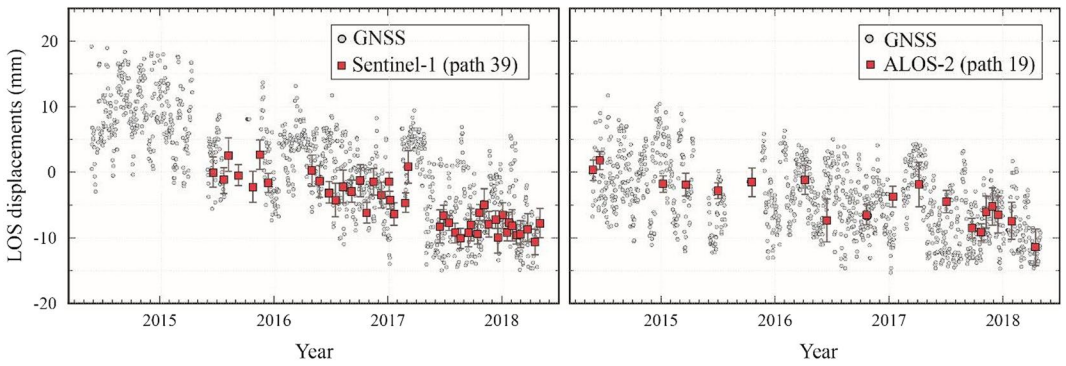

Fig. 11 Comparisons of displacement time series between InSAR measurements (red squares) and GNSS measurements (gray circles) at the KAHG GNSS site. The GNSS 3D displacement components are, respectively, projected into the LOS directions of **a** ascending Sentinel-1 (path 39), and **b** the descending ALOS-2 (path 19) for comparisons. Error bars indicate the estimated uncertainties of InSAR measurements similar to these in Fig. 9

depressurization cycles. Moreover, these ground-based measurements were primarily conducted far from the summit, while our InSAR measurements mainly cover the summit region and the upper flanks. The deformation induced by inflation or deflation of the magma sources under Mt Asama may be spatially broad and are insensitive to our application of InSAR.

Possible mechanism for the observed deformation

As shown in "Results" section, we observed two deformed regions at the NEF and SEF of Asama volcano, respectively. In this section, we will inspect possible mechanisms to account for the observed deformation and highlight the importance of continuous deformation monitoring for mitigating future volcanic hazard at Mt Asama.

Possible mechanism for the deformation at NEF

The NEF of Asama volcano exhibits continuous subsidence during the whole period. Recent studies have shown that continuous subsidence at active volcanoes may be explained by several mechanisms such as magma withdrawal (e.g., Lu et al. 2010), consolidation of erupted deposits (e.g., Grapenthin et al. 2010), viscoelastic relaxation of the host rock (Yamasaki et al. 2018), thermal contraction of lava deposits or intruded magma body (e.g., Tallarico 2003; Wang and Aoki 2019), and the pore pressure drop associated with hydrothermal fluid circulations (Wauthier et al. 2018). We first excluded the magma withdrawal and viscoelastic relaxation, because these two mechanisms generally induce broadly symmetric deformation around the magma source, inconsistent with the observed deformation. Also, these two mechanisms produce deformation with a spatial scale broader than what we observe in this study.

Thermal contraction of the lava flow may be responsible for the observed subsidence. The geological map indicates that the NEF is covered by a lava flow region during the 1783 eruption. Yasui and Koyaguchi (2004) estimated the thickness of lava deposits at NEF ranging from about 20 m at the flank to about 90 m near the summit. The amount of observed deformation is correlated with the thickness of the lava deposit (Fig. 8). The duration of thermoelastic contraction depends on the volume and depth of the source as well as the thermal diffusivity of the surrounding crust (Furuya 2005). Recent studies at Usu volcano in Japan have shown that it takes more than 160 years for the surface subsidence to become smaller than 1 mm/year if we assume a heat source with a volume of 5×10^6 m^3 at a depth of about 100 m, a temperature of 1000 K, and thermal diffusivity of 1×10^{-5} m^2/s. If we assume that the average thickness of the lava deposits is 50 m at the northeast summit of Asama volcano, the volume of the heat source is similar to the case above. We thus suggest that the thermoelastic contraction of the 1783 lava flow is unlikely to fully explain the subsidence at NEF of Asama, where subsidence with rates up to -10 mm/year is observed. Moreover, considering that meteorological precipitation and groundwater flow would accelerate the cooling process (Chaussard 2016; Wang and Aoki 2019), some other mechanism must also contribute to the observed subsidence at NEF of Asama.

Another possibility leading to the observed subsidence is a pore pressure drop related to hydrothermal activity beneath Asama volcano. Figure 12 shows a schematic view of magma transport beneath Asama volcano inferred from previous geodetic and seismic observations (Aoki et al. 2013), in which blue and red rectangles beneath Kurofu volcano represent old and recent magma intrusions, respectively. The old magma intrusions emplaced before 24,000 years ago possess higher density

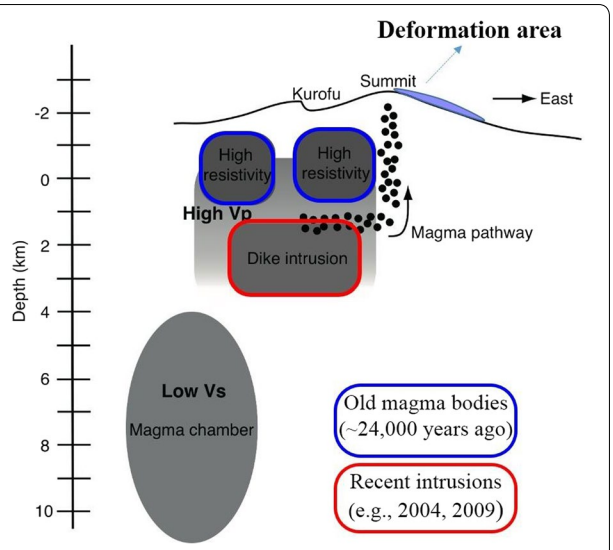

Fig. 12 A schematic view of potential magma pathway at Asama volcano inferred from geodetic and seismic studies. The black dots indicate the earthquake swarms recorded in the 2004 eruption (modified from Aoki et al. (2013))

than the recent intrusions due to slow cooling and thus prevent the magma in the deep reservoir from intruding upward directly but along the conduit toward the current crater (Fig. 11). This internal structure of Asama volcano results in a flow of hydrothermal fluid from depth to the east side of the volcano, where Usui et al. (2017) reported a porous layer with higher water content at a depth of ~ 1 km above sea level. Due to the lack of independent constraints from, say, the pressure, temperature, or fluid flux at Asama volcano, we were not able to conduct detailed modeling of the observed deformation to infer the properties of the hydrothermal system beneath the volcano. Assuming that the surface subsidence is entirely due to the loss of pore volume in the porous layer, the relationship between vertical subsidence (Δz) and porosity loss can be expressed as (Todesco et al. 2014).

$$\Delta z = z_0(\varepsilon_0 - \varepsilon)/(1 - \varepsilon) \quad (5)$$

where z_0 is the thickness of the porous rock layer, ε_0 and ε are the initial porosity and that after the porosity loss. We can estimate that a 1% loss of porosity in rock layer with a thickness of 50 m would cause surface subsidence of 213–495 mm with a typical initial porosity value of 0.3–0.5. Therefore, we argue that compaction of a porous layer at the east side of Asama volcano could be a possible reason for the observed subsidence at the NEF. Morita et al. (2016) reported that massive degassing of CO_2 was mainly observed at the eastern part of the summit of Asama volcano and suggested that the permeable zones connected to the deep hydrothermal fluid layer are responsible for the substantial degassing. The pore pressure drops may be triggered by changes in the feeding rate of magmatic gases at the base of the hydrothermal system or changes in permeability of the porous layer (Wauthier et al. 2018).

Possible mechanism of the deformation at SEF

We observed both vertical and horizontal displacements at the SEF of Asama volcano ("Results" section). LOS changes from the ascending path are much more apparent than from the descending path (Fig. 7), indicating that the surface moves mainly to the southeast in the slope direction. Considering the average slope angle at SEF of about 20°, we speculate that the displacements at SEF are due to slope instability. The geological map shows that SEF is covered by old lava deposits of Hotokeiwa volcano, which was active about 11,000 years ago. The linear deformation trend at SEF (Fig. 8d–f) indicates that the deformation there is likely a constant process at least in the latest decades or so although our InSAR observations only cover about 4 years.

Ongoing long-term flank motion at active volcanoes has been reported globally (e.g., Borgia et al. 2000; Di Traglia et al. 2014; Poland et al. 2017; Schaefer et al. 2019). Observations of flank instability at large basaltic volcanoes suggested that a weak substrate beneath the sliding surface should exist to accommodate persistent motion (Poland et al. 2017). Moreover, rates of flank motion are affected by several factors such as the magnitude of magma supply rate, the thickness of the substrate, and gravitational spreading of the edifice (Poland et al. 2017). However, the rock types at Hotokeiwa are dominated by dacite to rhyolite (Yasui 2018), which are much more viscous than basaltic, and little is known about the internal structure and deposit thicknesses of Hotokeiwa volcano. Therefore, inferring the properties of the sliding substrate is unrealistic from only our InSAR observations. Nonetheless, considering low magmatic activities at Asama without large surface deformation ("Comparison with historical deformation records at Asama volcano" section), we suggest that the gravitational loading on the SEF plays a key role in affecting the slope motion. The spreading of small horizontal velocity (< 10 mm/year) at the SEF also indicates that the depth of the sliding surface is deep seated. In contrast, surficial flank motions such as remobilization of volcanoclastic material and material erosion are typically localized and much faster (Schaefer et al. 2019).

Persistent deep-seated flank motion at active volcanoes is less likely to evolve into large-volume landslides, because elastic stress can be relaxed due to the very slow deformation rate (De Vries and Borgia 1996). This is justified by the absence of scarps or benches on the surface of the SEF at Mt Asama and no recording of large slope failure there. However, a sudden trigger to failure through the interaction of volcanic activity and slope instability is possible. Observations of flank instability at Stromboli volcano, Italy have shown that increase in magmatic pressurization may promote the sliding rate and eventually result in catastrophic failure along the preexisting shallow substrate (Di Traglia et al. 2014). Deep-seated flank motions evolving into debris avalanches can typically result in failure volume of more than 1×10^7 m^3, such as the debris avalanche at Mount St Helens in 1980 with volume of 2.5×10^9 m^3 (Glicken 1996), and at Soufriere Hills volcano in 2003 with volume of 2.1×10^8 m^3 (Herd et al. 2005). We thus argue that close monitoring of the flank instability at the SEF of Asama volcano should be taken in the future, given the significant threat of the SEF to the infrastructure and communities downstream.

Conclusions

By combining persistent and distributed scatterers, we successfully obtained the surface deformation of Asama volcano for the first time with SAR satellites between 2014 and 2018. Dense measurement points on the summit and flanks reveal two deformation regions, which are located at the northeast and southeast flanks of the volcano with areas of about 3.68 km^2 and 2.14 km^2, respectively. The northeast flank exhibits vertical subsidence of up to -10 mm/year near the summit. The southeast flank exhibits both vertical and eastward displacements of about -2.1 and 6.7 mm/year, respectively. Temporal evolution of displacements at both the two deformation regions shows a nearly linear trend over the observation period, which is confirmed by the GNSS measurements.

We interpreted that the vertical subsidence at the northeast flank of Mt Asama is mainly due to the pore pressure drop of a porous layer related to the hydrothermal activity of the volcano. Although the northeast flank is on the lava deposits of the 1783 eruption, the thermal contraction is likely minor after more than 200 years since lava emplacement. Considering the presence of both vertical and horizontal displacements at the southeast flank, we argue that flank instability is responsible for the deformation there. Continuous monitoring of the southeast flank of Asama volcano is necessary considering an existing weaker layer at a shallow depth may be responsible for flank instability and be stimulated by a future eruption.

Supplementary information

Supplementary information accompanies this paper at https://doi.org/10.1186/s40623-019-1104-9.

Additional file 1. Additional figures and tables.

Abbreviations

ADI: Amplitude dispersion index; DEM: Digital elevation model; DS: Distributed scatterers; GNSS: Global navigation satellite system; InSAR: Interferometric synthetic aperture radar; LOS: Line of sight; NDVI: Normalized Difference Vegetation Index; NEF: Northeast flank; PS: Persistent scatterers; SEF: Southeast flank; SHPs: Statistically homogeneous pixels; StaMPS: Stanford Method for Persistent Scatterers; TRAIN: Toolbox for Reducing Atmospheric InSAR Noise; VEI: Volcanic Explosivity Index.

Acknowledgements

This work is supported by Integrated Program for Next Generation Volcano Research and Human Resource Development Japan. The authors would thank Zhenhong Li for providing the GACOS atmospheric phase delay products. Parts of the figures were created by Generic Mapping Tools (Wessel et al. 2013).

Authors' contributions

XW processed the SAR images and conducted the result analyzing, as well as written the draft paper. YA helped analyze and interpret the deformation, as well as revised the manuscript. JC contributed to the development of the codes for SAR data processing. All authors read and approved the final manuscript.

Funding

XW is supported by the National Natural Science Foundation of China (Grant No. 41804009).

Availability of data and materials

The Sentinel-1 SAR images are provided by the European Space Agency, which can be freely downloaded from https://scihub.copernicus.eu/. The ALOS-1/2 SAR data are shared among PIXEL (PALSAR Interferometry Consortium to Study our Evolving Land surface), and provided by the Japan Aerospace Exploration Agency (JAXA) under a cooperative research contract with the Earthquake Research Institute, The University of Tokyo. The ownership of PALSAR and PALSAR-2 data belongs to the Ministry of Economy, Trade, and Industry, and JAXA.

Ethics approval and consent to participate

Not applicable.

Consent for publication

Not applicable.

Competing interests

The authors declare that they have no competing interests.

Author details

[1] Earthquake Research Institute, The University of Tokyo, Tokyo, Japan. [2] Department of Surveying and Geo-Informatics, Faculty of Geosciences and Environmental Engineering, Southwest Jiaotong University, Chengdu, China. [3] Institute of Space and Earth Information Science, The Chinese University of Hong Kong, Hong Kong, China.

Received: 22 July 2019 Accepted: 1 November 2019
Published online: 14 November 2019

References

Aoki Y, Takeo M, Ohminato T, Nagaoka Y, Nishida K (2013) Magma pathway and its structural controls of Asama Volcano, Japan. Geol Soc 380:67–84. https://doi.org/10.1144/sp380.6

Aramaki S (1963) Geology of Asama volcano. J Fac Sci Univ Tokyo 2:229–443

Beauducel B, Briole P, Froger JL (2000) Volcano-wide fringes in ERS synthetic aperture radar interferograms of ETNA (1992–1998): deformation or tropospheric effect? J Geophys Res 105:16391–16402

Bekaert DPS, Walters RJ, Wright TJ, Hooper AJ, Parker DJ (2015) Statistical comparison of InSAR tropospheric correction techniques. Remote Sens Environ 170:40–47. https://doi.org/10.1016/j.rse.2015.08.035

Borgia A, Delaney PT, Denlinger RP (2000) Spreading volcanoes. Annu Rev Earth Planet Sci 28:539–570. https://doi.org/10.1146/annurev.earth.28.1.539

Cecchi GC (1991) Error analysis of the parameters of a least-squares determined curve when both variables have uncertainties. Meas Sci Technol 2:1127–1128. https://doi.org/10.1088/0957-0233/2/12/001

Chaussard E (2016) Subsidence in the Parícutin lava field: causes and implications for interpretation of deformation fields at volcanoes. J Volcanol Geoth Res 320:1–11. https://doi.org/10.1016/j.jvolgeores.2016.04.009

Cigna F, Bateson LB, Jordan CJ, Dashwood C (2014) Simulating SAR geometric distortions and predicting Persistent Scatterer densities for ERS-1/2 and ENVISAT C-band SAR and InSAR applications: nationwide feasibility assessment to monitor the landmass of Great Britain with SAR imagery. Remote Sens Environ 152:441–466. https://doi.org/10.1016/j.rse.2014.06.025

Crosetto M, Monserrat O, Cuevas-González M, Devanthéry N, Crippa B (2016) Persistent scatterer interferometry: a review. ISPRS J Photogram Remote Sens 115:78–89. https://doi.org/10.1016/j.isprsjprs.2015.10.011

Dee DP, Uppala SM, Simmons AJ, Berrisford P, Poli P, Kobayashi S, Vitart F (2011) The ERA-Interim reanalysis: configuration and performance of the data assimilation system. Quart J R Meteorol Soc 137:553–597. https://doi.org/10.1002/qj.828

De Vries BVW, Borgia A (1996) The role of basement in volcano deformation. Geol Soc 110:95–110. https://doi.org/10.1144/GSL.SP.1996.110.01.07

Di Traglia F, Nolesini T, Intrieri E, Mugnai F, Leva D, Rosi M, Casagli N (2014) Review of ten years of volcano deformations recorded by the ground-based InSAR monitoring system at Stromboli volcano: a tool to mitigate volcano flank dynamics and intense volcanic activity. Earth Sci Rev 139:317–335. https://doi.org/10.1016/j.earscirev.2014.09.011

Efron B, Tibshirani R (1986) Bootstrap methods for standard errors, confidence intervals, and other measures of statistical accuracy. Stat Sci. 1:54–77. https://doi.org/10.1214/ss/1177013815

Ferretti A, Prati C, Rocca F (2001) Permanent scatterers in SAR interferometry. IEEE Trans Geosci Remote Sens 39:8–20. https://doi.org/10.1109/36.898661

Ferretti A, Fumagalli A, Novali F, Prati C, Rocca F, Rucci A (2011) A new algorithm for processing interferometric data-stacks: squeeSAR. IEEE Trans Geosci Remote Sens 49:3460–3470. https://doi.org/10.1109/tgrs.2011.2124465

Furuya M (2005) Quasi-static thermoelastic deformation in an elastic half-space: theory and application to InSAR observations at Izu-Oshima volcano, Japan. Geophys J Int 161:230–242. https://doi.org/10.1111/j.1365-246X.2005.02610.x

Glicken H (1996) Rockslide-debris avalanche of May 18, 1980, Mount St. Helens volcano, Washington. US Geological Survey (Open File Report), 96–677. https://doi.org/10.3133/ofr96677

Grapenthin R, Ófeigsson BG, Sigmundsson F, Sturkell E, Hooper A (2010) Pressure sources versus surface loads: analyzing volcano deformation signal composition with an application to Hekla volcano, Iceland. Geophys Res Lett. https://doi.org/10.1029/2010GL044590

Hayakawa Y (2006) Aerial view of Asama Volcano from the NE. J Geogr. https://doi.org/10.5026/jgeography.115.2_Plate1 **(in Japanese)**

Herd RA, Edmonds M, Bass VA (2005) Catastrophic lava dome failure at Soufrière Hills volcano, Montserrat, 12–13 July 2003. J Volcanol Geotherm Res. 148:234–252

Hooper A (2008) A multi-temporal InSAR method incorporating both persistent scatterer and small baseline approaches. Geophys Res Lett. https://doi.org/10.1029/2008gl034654

Hooper A, Zebker H, Segall P, Kampes B (2004) A new method for measuring deformation on volcanoes and other natural terrains using InSAR persistent scatterers. Geophys Res Lett. https://doi.org/10.1029/2004gl021737

Hooper A, Bekaert D, Spaans K, Arıkan M (2012) Recent advances in SAR interferometry time series analysis for measuring crustal deformation. Tectonophysics 514–517:1–13. https://doi.org/10.1016/j.tecto.2011.10.013

Jiang M, Ding X, Hanssen RF, Malhotra R, Chang L (2015) Fast statistically homogeneous pixel selection for covariance matrix estimation for multitemporal InSAR. IEEE Trans Geosci Remote Sens 53:1213–1224. https://doi.org/10.1109/tgrs.2014.2336237

Kazahaya R, Aoki Y, Shinohara H (2015) Budget of shallow magma plumbing system at Asama volcano, Japan, revealed by ground deformation and volcanic gas studies. J Geophys Res 120:2961–2973. https://doi.org/10.1002/2014JB011715

Kinoshita Y, Furuya M, Hobiger T, Ichikawa R (2012) Are numerical weather model outputs helpful to reduce tropospheric delay signals in InSAR data? J Geodesy 87:267–277. https://doi.org/10.1007/s00190-012-0596-x

Lu Z, Dzurisin D, Biggs J, Wicks C, McNutt S (2010) Ground surface deformation patterns, magma supply, and magma storage at Okmok volcano, Alaska, from InSAR analysis: 1. Intereruption deformation, 1997–2008. J Geophys Res. https://doi.org/10.1029/2009jb006969

Morita M, Mori T, Kazahaya R, Tsuji H (2016) Diffuse carbon dioxide emissions from hidden subsurface structures at Asama volcano, Japan. Bull Volcanol. https://doi.org/10.1007/s00445-016-1008-5

Murase M, Ono K, Ito T, Miyajima R, Mori H, Aoyama H, Fujii N (2007) Time-dependent model for volume changes in pressure sources at Asama volcano, central Japan due to vertical deformations detected by precise leveling during 1902–2005. J Volcanol Geoth Res 164:54–75. https://doi.org/10.1016/j.jvolgeores.2007.04.001

Murray KD, Bekaert DPS, Lohman RB (2019) Tropospheric corrections for InSAR: statistical assessments and applications to the Central United States and Mexico. Remote Sens Environ 232:111326. https://doi.org/10.1016/j.rse.2019.111326

Newhall CG, Self S (1982) The Volcano Explosivity Index (VEI): an estimate of explosive magnitude for historical volcanism. J Geophys Res 87:1231–1238. https://doi.org/10.1029/JC087iC02p01231

Osmanoğlu B, Sunar F, Wdowinski S, Cabral-Cano E (2016) Time series analysis of InSAR data: methods and trends. ISPRS J Photogram Remote Sens 115:90–102. https://doi.org/10.1016/j.isprsjprs.2015.10.003

Papoulis A (1965) Probability, random variables and stochastic processes. McGraw-Hill, New York

Parizzi A, Brcic R (2011) Adaptive InSAR Stack Multilooking exploiting amplitude statistics: a comparison between different techniques and practical results. IEEE Geosci Remote Sens Lett 8:441–445. https://doi.org/10.1109/lgrs.2010.2083631

Pettitt AN (1976) A two-sample Anderson-Darling rank statistic. Biometrika 63:161–168

Pinel V, Hooper A, De la Cruz-Reyna S, Reyes-Davila G, Doin MP, Bascou P (2011) The challenging retrieval of the displacement field from InSAR data for andesitic stratovolcanoes: case study of Popocatepetl and Colima Volcano, Mexico. J Volcanol Geoth Res 200:49–61. https://doi.org/10.1016/j.jvolgeores.2010.12.002

Pinel V, Poland MP, Hooper A (2014) Volcanology: lessons learned from synthetic aperture radar imagery. J Volcanol Geoth Res 289:81–113. https://doi.org/10.1016/j.jvolgeores.2014.10.010

Poland MP, Peltier A, Bonforte A, Puglisi G (2017) The spectrum of persistent volcanic flank instability: a review and proposed framework based on Kīlauea, Piton de la Fournaise, and Etna. J Volcanol Geoth Res 339:63–80. https://doi.org/10.1016/j.jvolgeores.2017.05.004

Rouse JW, Haas RH, Scheel JA, Deering, DW (1974) Monitoring vegetation systems in the great plains with ERTS. In: Proceedings, 3rd Earth Resource Technology Satellite (ERTS) Symposium 1, p. 48–62

Remy D, Chen Y, Froger JL, Bonvalot S, Cordoba L, Fustos J (2015) Revised interpretation of recent InSAR signals observed at Llaima volcano (Chile). Geophys Res Lett 42:3870–3879. https://doi.org/10.1002/2015gl063872

Schaefer LN, Di Traglia F, Chaussard E, Lu Z, Nolesini T, Casagli N (2019) Monitoring volcano slope instability with Synthetic Aperture Radar: a review and new data from Pacaya (Guatemala) and Stromboli (Italy) volcanoes. Earth Sci Rev 192:236–257. https://doi.org/10.1016/j.earscirev.2019.03.009

Shamshiri R, Nahavandchi H, Motagh M, Hooper A (2018) Efficient ground surface displacement monitoring using Sentinel-1 data: integrating distributed scatterers (DS) identified using two-Sample T-test with persistent scatterers (PS). Remote Sens 10:794. https://doi.org/10.3390/rs10050794

Stephens MA (1970) Use of the Kolmogorov-Smirnov, Cramér-Von Mises and related statistics without extensive tables. J R Stat Soc Ser B 32:115–122

Takeo M, Aoki Y, Ohminato T, Yamamoto M (2006) Magma supply path beneath Mt. Asama Volcano, Japan. Geophys Res Lett 33:15310. https://doi.org/10.1029/2006gl026247

Tallarico A (2003) Modeling long-term ground deformation due to the cooling of a magma chamber: case of Basiluzzo island, Aeolian Islands, Italy. J Geophys Res. https://doi.org/10.1029/2002jb002376

Tizzani P, Berardino P, Casu F, Euillades P, Manzo M, Ricciardi G, Lanari R (2007) Surface deformation of Long Valley caldera and Mono Basin, California, investigated with the SBAS-InSAR approach. Remote Sens Environ 108:277–289. https://doi.org/10.1016/j.rse.2006.11.015

Todesco M, Costa A, Comastri A, Colleoni F, Spada G, Quareni F (2014) Vertical ground displacement at Campi Flegrei (Italy) in the fifth century: rapid subsidence driven by pore pressure drop. Geophys Res Lett 41:1471–1478. https://doi.org/10.1002/2013GL059083

Tsunematsu N, Nagai T, Murayama T, Adachi A, Murayama Y (2008) Volcanic ash transport from mount Asama to the Tokyo metropolitan area influenced by large-scale local wind circulation. J Appl Meteorol Climatol 47:1248–1265. https://doi.org/10.1175/2007jamc1644.1

Usui Y, Ogawa Y, Aizawa K, Kanda W, Hashimoto T, Koyama T, Kagiyama T (2017) Three-dimensional resistivity structure of Asama Volcano revealed by data-space magnetotelluric inversion using unstructured tetrahedral elements. Geophys J Int 208:1359–1372. https://doi.org/10.1093/gji/ggw459

Wang X, Aoki Y (2019) Posteruptive thermoelastic deflation of intruded Magma in Usu Volcano, Japan, 1992–2017. J Geophys Res 124:335–357. https://doi.org/10.1029/2018JB016729

Wauthier C, Smets B, Hooper A, Kervyn F, d'Oreye N (2018) Identification of subsiding areas undergoing significant magmatic carbon dioxide degassing, along the northern shore of Lake Kivu, East African Rift. J Volcanol Geoth Res 363:40–49. https://doi.org/10.1016/j.jvolgeores.2018.08.018

Wegmüller U, Werner CL (1997) Gamma SAR processor and interferometry software, Proc. the 3rd ERS Symposium, ESA, Florence, Italy, pp. 1686–1692

Wessel P, Smith WHF, Scharroo R, Luis J, Wobbe F (2013) Generic Mapping Tools: improved Version Released. Eos Trans Am Geophys Union 94:409–410. https://doi.org/10.1002/2013EO450001

Wright TJ, Parsons BE, Lu Z (2004) Toward mapping surface deformation in three dimensions using InSAR. Geophys Res Lett. https://doi.org/10.1029/2003GL018827

Yamasaki T, Kobayashi T, Wright TJ, Fukahata Y (2018) Viscoelastic crustal deformation by magmatic intrusion: a case study in the Kutcharo caldera, eastern Hokkaido, Japan. J Volcanol Geoth Res 349:128–145. https://doi.org/10.1016/j.jvolgeores.2017.10.011

Yasui M (2018) Textures of the Eruptive Products of Asama-Maekake Volcano from the 12th Century: Indicator of Eruptive Processes. Proceedings of the Institute of Natural Sciences, Nihon University. pp. 37-50

Yasui M, Koyaguchi T (2004) Sequence and eruptive style of the 1783 eruption of Asama Volcano, central Japan: a case study of an andesitic explosive eruption generating fountain-fed lava flow, pumice fall, scoria flow and forming a cone. Bull Volcanol 66:243–262. https://doi.org/10.1007/s00445-003-0308-8

Yu C, Li Z, Penna NT, Crippa P (2018) Generic atmospheric correction model for interferometric synthetic aperture radar observations. J Geophys Res 123:9202–9222. https://doi.org/10.1029/2017JB015305

Zebker HA, Werner CL, Rosen PA, Hensley S (1994) Accuracy of topographic maps derived from ERS-1 interferometric radar. IEEE Trans Geosci Remote Sens 32:823–836. https://doi.org/10.1109/36.298010

Publisher's Note